J. Micromech. Microeng. **23** (2013) 025016 (11pp) doi:10.1088/0960-1317/23/2/025016

Investigation of the maskless lithography technique for the rapid and cost-effective prototyping of microfluidic devices in laboratories

Nan Xiang[1,2], **Hong Yi**[1,2], **Ke Chen**[1,2], **Shanfang Wang**[1,2] **and Zhonghua Ni**[1,2,3]

[1] School of Mechanical Engineering, Southeast University, Nanjing 211189, People's Republic of China
[2] Jiangsu Key Laboratory for Design and Manufacture of Micro-Nano Biomedical Instruments, Nanjing 211189, People's Republic of China

E-mail: nzh2003@seu.edu.cn

Received 22 October 2012, in final form 30 November 2012
Published 9 January 2013
Online at stacks.iop.org/JMM/23/025016

Abstract
This paper describes maskless lithography as a rapid and cost-effective technique for fabricating high-quality microfluidic devices in laboratories. The detailed effects of exposure parameters on microstructure features are explored. A quantitative analysis of these effects provides insights into the device design and the selection of optimum processing parameters. To overcome the limitation of small exposure area, subregion stitching and sequential exposure are adopted for fabricating larger patterns. Seamless stitching between adjacent exposure subregions is achieved by optimizing the grayscale values of the stitching side/corner. These data are also valuable for exploring grayscale and multi-step lithography. Various hydrodynamic microdevices are then fabricated and characterized to validate the optimized parameters.

(Some figures may appear in colour only in the online journal)

1. Introduction

As an advanced technique for exploring new physical mechanisms on the micro/nano-scale or realizing novel application functions, microfluidics has attracted increasing interests due to its unique advantages such as reduced consumption of samples and reagents, potential for increased efficiency and small volume. The explosive growth in the demand of microfluidic devices with more complex and finer morphology, lower fabrication cost and shorter development cycle poses a great challenge to the microfabrication field. Although the conventional fabrication scheme for microelectromechanical systems (MEMS) has gone through significant development, a more rapid and inexpensive technique for fabricating prototype microfluidic devices is in urgent demand in laboratories where prototype devices are heavily consumed and frequent modifications of design specifications are inevitable.

In an attempt to meet this demand, various types of one-step or multi-step manufacturing techniques have been developed to prototype microfluidic devices with different dimensions and cross-sectional shapes [1–4]. Materials for fabricating microfluidic devices have also evolved from expensive glass/silicon [5, 6] to polymer, tape and paper [7, 8], significantly reducing the time, cost and complexity of prototyping. Among these fabrication schemes, the polydimethylsiloxane (PDMS)-based soft lithography has been most widely utilized in the microfluidic community due to its distinctive advantages such as high replication fidelity, ease of fabrication and bonding, low cost and the excellent material properties of PDMS itself [9–11]. For implementing this scheme, the preparation of a master mold is critical for the production of PDMS replicas. Although

[3] Author to whom any correspondence should be addressed.

the emergence of various non-lithographic patterning methods provides researchers with a broader choice for the fabrication of a master mold [12–14], lithography is still one of the simplest and most straightforward methods employed in laboratories.

However, traditional lithography approaches suffer from a lack of high efficiency and a difficulty of implementation in rapid prototyping due to their use of expensive and time-consuming chrome masks. A simple approach to overcome this drawback is to replace the glass/metal mask with the transparency mask produced by a high-resolution printer [10, 11]. However, the resolution of this method is less than adequate for most microfluidic research works. Some research works have reported attempts to reform the mold fabrication methods from aspects of exposure light source [15], fabrication process [16] and materials of the substrate and mold [17, 18], which are promised to be valuable for laboratories with low hardware configurations. Unfortunately, these approaches cannot avoid the problems arising from the use of physical masks.

Digital micro-mirror device (DMD)-based maskless lithography can selectively and flexibly modulate the spatial UV light for patterning according to the pixel information of the image masks loaded in a computer. Serving as a virtual mask, the projected UV micropattern can be rapidly reconfigured and output various shades of gray in a single exposure. Moreover, this approach achieves a good balance between the fabrication cost, the cycle time and the resolution, promising to be a rapid and cost-effective fabrication method with an acceptable resolution for laboratory use. Due to the small coverage area of a single exposure, however, this approach has mostly been used in nano/biomaterials patterning [19, 20], light-directed fabrication of DNA microarrays [21, 22], real-time synthesis of microstructures or microparticles [23–25] and grayscale fabrication of three-dimensional microstructures [26, 27], but rarely in microfluidic device preparation. Okano's group [28, 29] developed a maskless lithography device by modifying a commercial liquid crystal display projector, realizing the fabrication of simple microchannels for cell patterning. Zhao *et al* [30] used the software alignment function of a direct projection lithography system and the plasma-assisted thermal lamination bonding technique to fabricate multilayer three-dimensional microstructures. Leigh *et al* [31] utilized a microscope integrated with a programmable stage to fabricate microstructures with feature sizes in the sub-millimeter range. However, systematic studies disclosing detailed effects of the critical processing parameters on microstructure features are still lacking. The quantitative characterization and analysis of these effects can provide insights into the device design and the selection of the best fabrication processing parameters for specific microfluidic application purposes. Moreover, a detailed knowledge on how to achieve seamless stitching between adjacent exposure subregions is of critical importance for fabricating larger microstructures, but has not been reported so far.

In this work, we performed a systematic experimental investigation of the critical processes and techniques involved in the application of maskless lithography as a rapid and cost-effective method for fabricating prototype microfluidic devices in laboratories. The selection and optimization of these corresponding parameters were in accordance with the unique characteristics of both microfluidics and maskless lithography. Specifically, the effects of exposure parameters on microstructure features were systematically explored. Then, the subregion stitching technique and sequential exposure process were adopted to fabricate larger patterns and the effects of stitching parameters on the stitching quality were studied. Finally, based on the obtained optimum processing parameters, several types of hydrodynamic microdevices were successfully fabricated and validated.

2. Materials and methods

2.1. Working principle of the lithography platform

Exposure experiments in this work were carried out on the basis of a simple exposure platform (SF-100 XTREME) from Intelligent Micro Patterning LLC. The block diagram and software configuration of this platform are schematically illustrated in figure 1. Its working principle is briefly overviewed as follows.

Firstly, the poly-chromatic light emanating from a 200 W mercury arc lamp is efficiently transferred to the optical train which consists of a field lens, a condenser lens and other optical components for light collimation and uniformity. The motorized filter wheel is used for generating specific exposure wavelengths (g-line (435 nm), h-line (405 nm) and i-line (365 nm)) or removing the UV energy (the wavelength λ <510 nm) to avoid the non-normal exposure during the auto-focusing and aligning procedures.

Secondly, the produced light spectrum is reflected by a mirror onto the 'Smart Filter', the key module of this system. The critical component of this module is the DMD comprised of 1024 × 768 micromirrors. These micromirrors are individually controlled according to the pixel information of the image mask. Each micromirror has two position states: ON and OFF. In the ON state, a micromirror reflects the light onto the substrate through the rest optics, transferring a bright pixel. In the OFF state, the micromirror directs the light elsewhere, making the pixel appear dark. These micromirrors can be toggled between ON and OFF states at a specific frequency to generate grayscale patterns. The toggling frequency denoting the ratio of ON time to OFF time determines the gray shades produced.

Finally, the light pattern is projected through an imaging lens and an infinity lens, reflected by a beam splitter and then reduced by an objective lens. The fixed imaging lens (2:1 reduction) is designed to form a reduced image of the exposure pattern. The use of infinity tube lens permits the insertion of a beam splitter into the generated parallel optical path. In addition, this whole procedure ensures that the final micropattern projected onto the substrate is free of distortion and remains uniform throughout the whole exposure area. Three objective lenses with different magnifications (4×, 10× and 20×) are equipped to achieve different

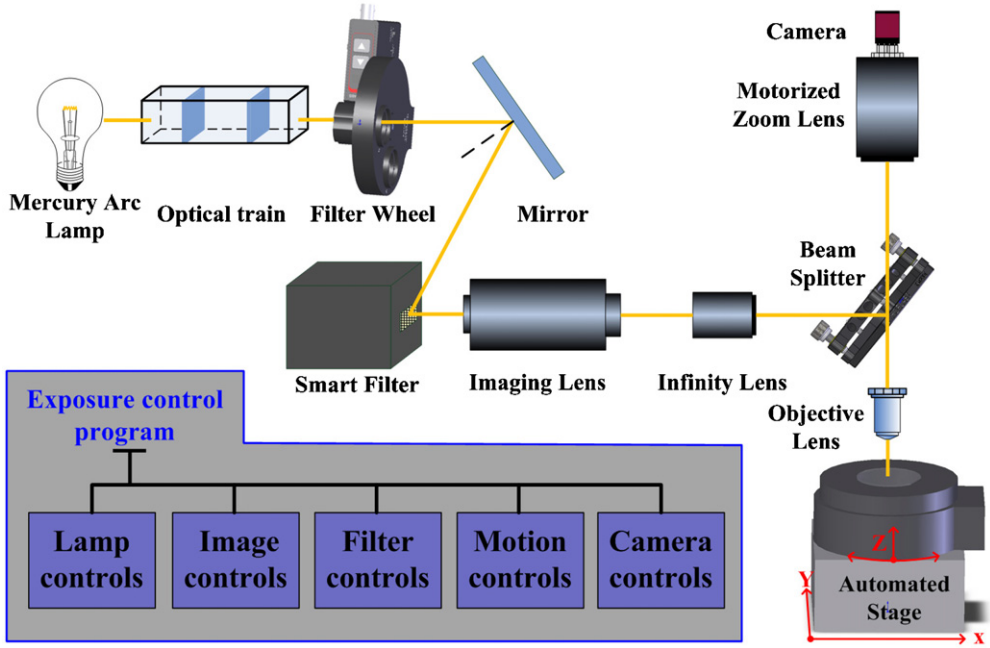

Figure 1. Block diagram and software configuration of the maskless lithography system.

numerical apertures (NA = 0.13, 0.30 and 0.45) and pixel resolutions (1.25, 0.5 and 0.25 μm) for specific application purposes. Responsible for controlling the horizontal and vertical movements of the substrate, the high-precision stage realizes the in-focus imaging of the micropattern at the surface of the photoresist film and the dynamic switching among exposure subregions. By coupling the micropattern projecting optical path with another observation optical path consisting of a beam splitter, a motorized zoom lens and a camera, the imaging quality of image masks on the substrate can be visualized in real-time. Meanwhile, an exposure control program is used to implement collaborative control of all functional components to accomplish the whole exposure process.

2.2. Image mask design and generation

Using AutoCAD 2010 (AutoDesk, Inc.), the mask designs were drawn at their actual sizes and exported as monochrome BMP format images. The white sections of these image masks represent the exposure zones; the size of each image pixel is dependent on the magnification of the objective lens equipped in the maskless lithography system. In this work, we chose a 4 × objective lens (Plan Fluor 4 × /0.13, Nikon) to obtain a pixel size of 1.25 μm × 1.25 μm. This resolution is adequate for most microfluidic applications. Although using objective lenses with higher magnification and numerical aperture (NA) may further enhance the fabrication accuracy, the increase of the numerical aperture will result in the decrease of the photoresist's thickness to compensate for the smaller depth of focus (DOF). The exported image mask was then loaded directly into the maskless lithography system to control the states of micromirrors in the DMD for selectively modulating the exposure light.

2.3. Fabrication process of SU-8 microstructures

Taking into account the demand of deep microcavities and the wide use of SU-8 negative photoresists in microfluidic research works, we applied SU-8 2050 (MicroChem Corp.) to achieve a 50 μm thick film across the 4″ single-side polished silicon wafer for the following exposure experiments. As shown in figure 2(*a*), the detailed process for fabricating the SU-8 master mold involves several critical operation steps including substrate pretreatment (surface cleaning and dehydration), spin coating of the photoresist, soft baking, exposure, post-exposure baking and developing. The multi-step spin coating procedure was conducted by using an automatic spin coater (LSM-250-BM, Sawatec AG). After soft baking, the wafer was cut into small pieces with acceptable dimensions so that the cost of a single fabrication run and the time consumption of the following development cycle can be further reduced. The i-line UV light (λ = 365 nm) was selected as the light source to pattern the thick SU-8 photoresist film due to its high sensitiveness. The UV intensity analyzer (Model 356, OAI) was used for the precise measurement of the exposure energy and intensity at the surface of the photoresist film. The soft baking and post-exposure baking steps were carried out on a hot plane (KW-4AH, Chemat Technology, Inc.) at 65 and 95 °C, respectively. Finally, the uncured photoresist was dissolved by using the SU-8 developer (PGMEA, MicroChem Corp.), obtaining the desired microstructure patterns.

2.4. Quantitative measurement and characterization of the microstructures

The obtained microstructures were observed and captured through an upright microscope (Eclipse 50i, Nikon) equipped with a color CCD camera (DXM1200F, Nikon). It is worth

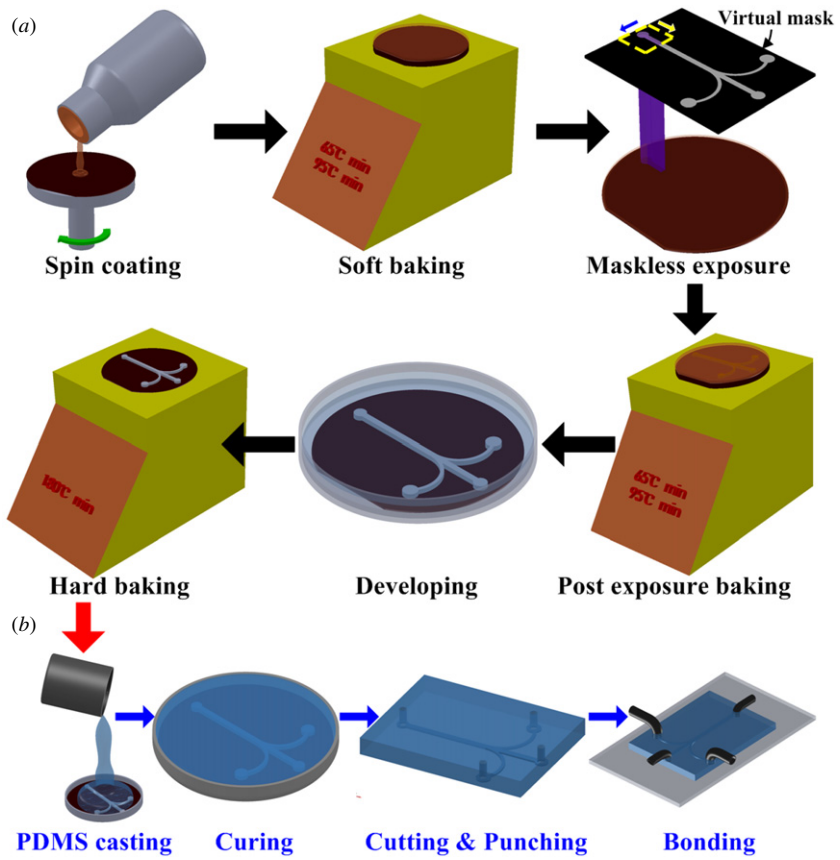

Figure 2. Schematic illustration of the process for fabricating PDMS-based microfluidic devices using maskless lithography: (*a*) procedure for fabricating the SU-8 master mold and (*b*) procedure for PDMS casting and device packaging.

mentioning that the microstructure images obtained from the single-type exposure experiment were captured at the same focal plane of this microscope so that the effects of specific processing parameters on microstructure features can be precisely studied. Then, the calibrated ImageJ software (NIH, USA) was used to quantify the detailed dimensions of the microstructures and characterize the grayscale values across the stitching regions. The microstructure features in the vertical direction were visualized by a scanning electron microscopy (Helios Nanolab 600, FEI). The PDMS casting technique was employed to replicate the microstructures for characterizing their cross-sectional features or verifying their functions. A schematic diagram of this process can be seen in figure 2(*b*). Briefly, the PDMS prepolymer and curing agent (Sylgard 184, Dow Corning Corp.) were thoroughly mixed at a ratio of 10:1 w/w, poured onto the SU-8 master mold, degassed under vacuum and cured at 80 °C for 2 h. After curing, the PDMS replica was peeled from the master mold, and the holes were punched. Then, the PDMS replica was permanently bonded to a glass slide through UV/Ozone treatment (144AX-220, Jelight Company, Inc.). Features of the final PDMS device were characterized through an inverted microscope (IX 71, Olympus) equipped with a 14 bit monochrome CCD camera (Exi Blue, Qimaging).

3. Results and discussion

3.1. Effects of exposure time on microstructure features

The exposure dose is an important factor that significantly affects the features of the lithographically patterned microstructures. Its value, which can be given by the product of light intensity and exposure time, is dependent on the lithography system, photoresist type and film thickness. For a specific lithography system, the overall light intensity remains unchanged within a certain time bound (for the system used in this work, the measured light intensity at the surface of the photoresist is $\sim$10 mW cm^{-2}). Thus, the determination of the exposure time is a prerequisite for successful and efficient fabrication of microfluidic devices.

In order to quantitatively characterize the effects of exposure time on microstructure quality and dimension, we utilized image masks (800 pixels $\times$ 656 pixels) consisting of a line array with varied width, as are illustrated in figures 3(*a*) and (*b*), to conduct the exposure experiments. By considering the resolution limit due to diffraction (R) $\sim$3 μm ($R = K\lambda/\mathrm{NA}$, where the parameter K is $\sim$1 for a single-layer photoresist on a reflective substrate [32]) and the loss of accuracy caused by the error of actual optical path and the refraction at the air/photoresist interface, the linewidths of the microstructure array were designed to increase from 5 to 65 μm with an interval of 5 μm (the spacing between two

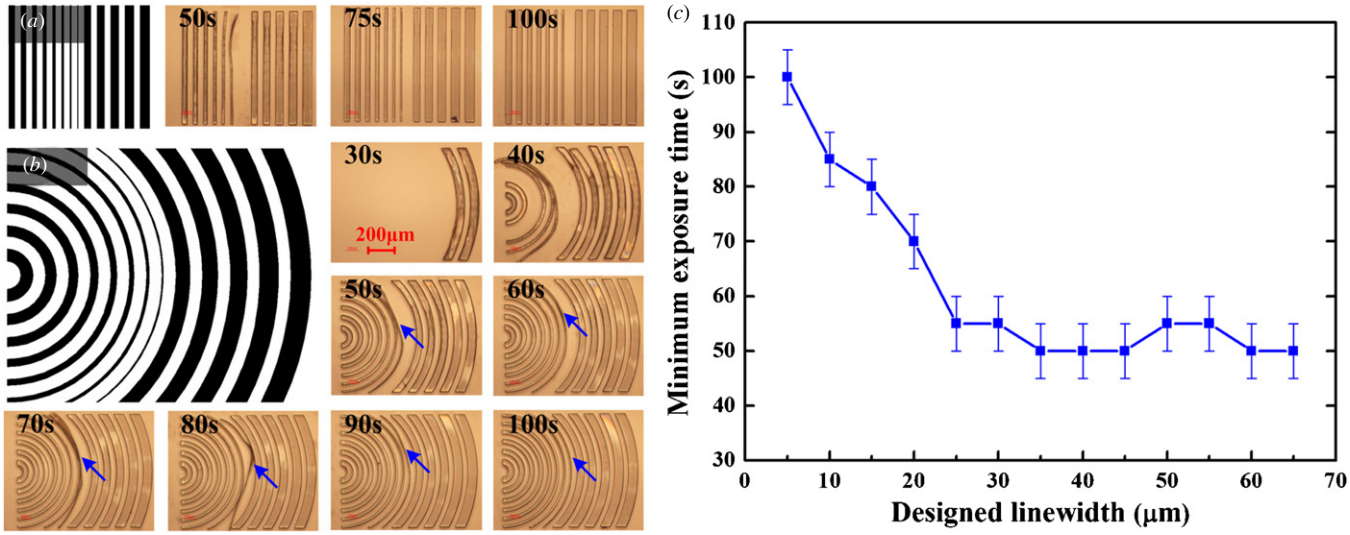

Figure 3. Effects of exposure time on the microstructure quality. (*a*) Reversed monochrome image mask consisting of a straight-line array with varied width and selected microscopic images of microstructures fabricated under an exposure time of 50, 75 and 100 s, respectively. The linewidth is 40–5 μm and 45–65 μm from left to right with an interval of 5 μm. The spacing between two adjacent lines is constant at 40 μm. (*b*) Optimized mask design (the configuration and dimension are the same with the above mask design), and selected microscopic images of microstructures fabricated under exposure times of 30–100 s (with an interval of 10 s). Microstructures with a linewidth of 5 μm are marked with blue arrows in this figure. (*c*) The curve illustrating the relationship between minimum exposure time and designed linewidth of microstructures.

adjacent lines was constant at 40 μm). The corresponding aspect ratio (AR) ranged from 0.77 to 10. In addition, we ran an exposure time series on the same substrate to ensure that other processing parameters remained constant. Exposure time, the only variable, was gradually increased from 30 to 100 s with an interval of 5 s.

Figure 3(*a*) shows the microscopic images selected from the above exposure experiment. As can be seen in this figure, the quality of the microstructures is significantly improved with increasing exposure time. However, the 5 μm lines are all detached from the substrate due to the relatively high aspect ratio (AR = 10). In an effort to overcome this problem, we introduced curvature to our mask design (figure 3(*b*)), increasing the lodging resistance of the microstructures. The microscopic images obtained from the exposure experiment using this improved mask design are also depicted in figure 3(*b*). This optimization can efficiently mitigate the collapse of high aspect ratio microstructures. We performed repeated exposure experiments using these masks, and then characterized and evaluated the actual dimension and quality of microstructures obtained under different exposure times. The results show that the microstructure quality is unacceptable when the exposure time is below 50 s due to insufficient cross-linking. Most importantly, we found that the microstructure quality seems to be dependent on the characteristic dimension of the microstructure (linewidth, in this work). Thus, we defined the shortest exposure time required for fabricating an acceptable microstructure of a certain linewidth as the minimum exposure time. The relationship between characteristic dimension (the designed linewidth) and minimum exposure time is established in figure 3(*c*) by evaluating the surface and contour properties of the microstructures. An important conclusion can be drawn from this curve that microstructures with smaller designed linewidths require relatively longer minimum exposure times. Specifically, in this work, the minimum exposure time required for fabricating microstructures with a linewidth of 5 μm is ~100 s. Comparatively, the minimum exposure time is constant at 50–60 s when the designed linewidth is larger than 25 μm. The cause for this difference is that the light intensity distribution of the projected line pattern at the image plane is linewidth dependent [33]. The peak intensity will gradually increase to be saturated at the maximum value (the overall intensity of this system, ~10 mW cm^{-2}) with the increase of the linewidth. In addition, it is known that the curing depth of the photoresist film is positively related to the local exposure intensity under a constant exposure time, i.e. with the decrease of the linewidth, the curing depth will decrease as well. In order to obtain better quality microstructure, a longer exposure time is required for smaller linewidth microstructure.

The exposure dose not only affects the cross-link density and the microstructure's surface and contour properties, but also significantly influences the microstructure's cross-sectional profile and dimensional accuracy. Hence, the use of minimum exposure time may suffer from disadvantages such as side-wall taper angle and dimensional deviation. However, for most microfluidic applications, microcavities are only used for transportation, mixing and reaction of biochemical reagents or separation and capturing of micro/nanomaterials [34, 35]. These applications typically do not require perfect side-wall verticality or strict dimension accuracy. Unlike conventional lithography methods that use the single-exposure mode, the maskless lithography method used in this work accomplishes the fabrication of larger patterns by applying subregion stitching and sequential exposure. As the whole

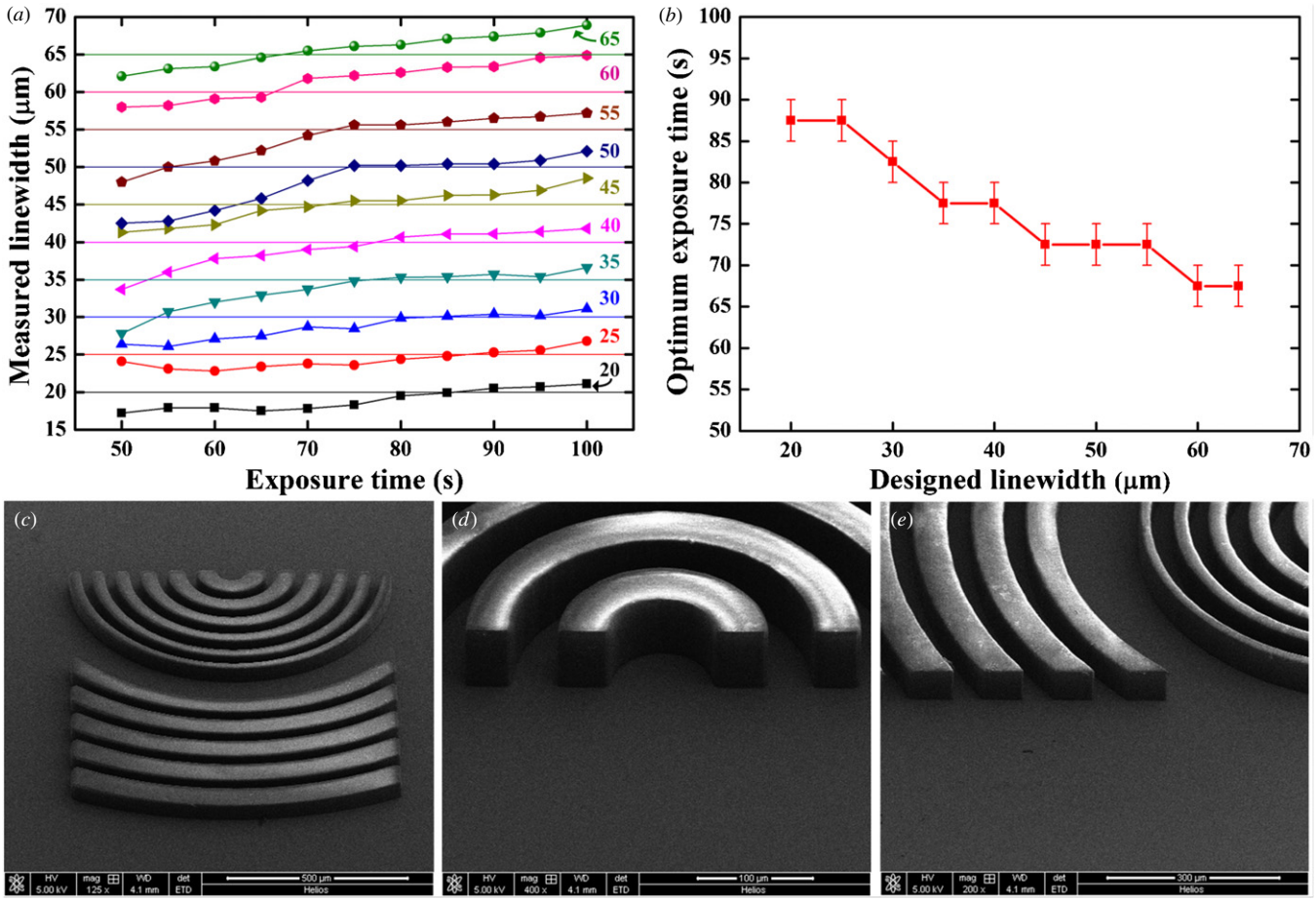

Figure 4. Effects of exposure time on microstructure dimension. (*a*) Curves illustrating the measured linewidths under various exposure times. The marked numbers beside the color curves indicate the designed linewidths of the microstructures. (*b*) Relationship between optimum exposure time and designed linewidth. (*c*)–(*e*) The SEM images of the microstructures' side-wall and cross-sectional profiles.

image mask may consist of hundreds or thousands of exposure subregions, the shorter time required for exposing a single subregion reduces the total time consumption for fabricating the integral device.

We further measured the actual dimension of microstructures with a designed linewidth of wider than 20 μm under various exposure times. Figure 4(*a*) shows the correlation between measured linewidth and exposure time. We observed that the measured linewidth increases gradually from lower than to larger than the designed linewidth along the increase of exposure time. This finding demonstrates that it is possible to fabricate microstructures of precise dimensions by carefully regulating the exposure time. In addition, the exposure time required for enabling the measured linewidth to be equal to the designed linewidth is defined as the optimum exposure time. It is found that the optimum exposure time is also determined by the characteristic dimension. The curve disclosing the detailed relationship between optimum exposure time and designed linewidth is illustrated in figure 4(*b*). As shown in this figure, the required optimum exposure time decreases significantly with increasing linewidth. For instance, the optimum exposure time for fabricating microstructures with a linewidth of 20 μm is 85–90 s, while it is reduced to 65–70 s with the linewidth coming up to 65 μm. In the meantime, the SEM images are used to verify that the side-wall profiles of the fabricated microstructures (exposure time 75 s, figure 4(*c*)–(*e*)) show quasi-perfect verticality under this exposure dose. A useful design rule can be derived from the above analyses that the exposure dose should be selected according to the minimum dimension in the mask design to further improve the fabrication efficiency and realize precise regulation of the microstructures' dimensions.

3.2. Key technologies for fabricating larger patterns

As mentioned above, the application of maskless lithography to microfluidic device fabrication is considerably constrained by the limitation of a single exposure's coverage area, which further decreases with the increase of the objective lens magnification. When using the 4 × objective lens, the dimension of a single exposure subregion is smaller than 1.28 mm × 0.96 mm, which is obviously not enough for microfluidic applications. To overcome this drawback, the subregion stitching scheme and sequential exposure process are used to fabricate larger patterns. Thus, exploring the optimum stitching parameters and understanding the influence of these parameters on the stitching quality are of great

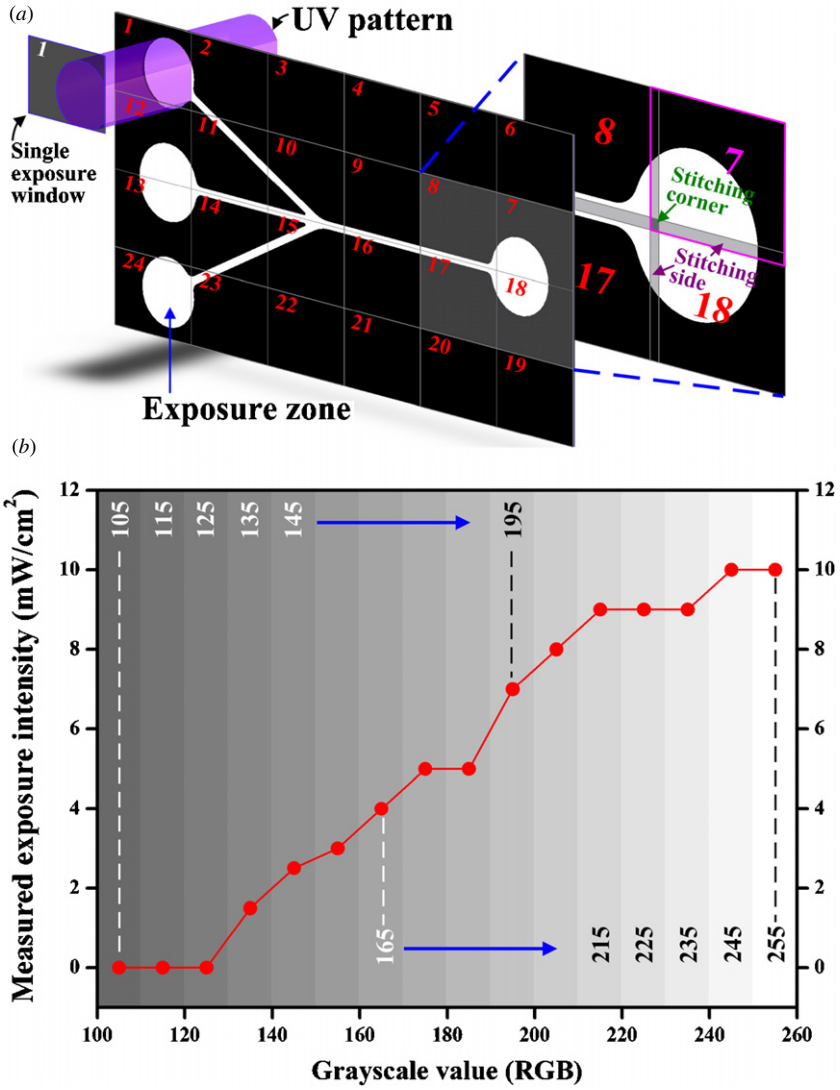

Figure 5. (*a*) Principles of sequential exposure and subregion stitching. The illustrated image mask is divided into 6 × 4 (24) subregions. The white regions on the mask represent the exposure zones. The exposure window moves across the mask in the marked order. (*b*) The curve illustrating the relationship between exposure intensity measured at the surface of the photoresist film and grayscale value of the loaded masks.

importance for utilizing maskless lithography to fabricate microfluidic devices. For a negative photoresist, in particular, the stitching quality directly affects the features of the microchannels' top surfaces.

Figure 5(*a*) schematically illustrates the sequential exposure and subregion stitching principles. Briefly, the whole mask is automatically divided into $m \times n$ subregions (the pixel dimension of each subregion is smaller than 1024 pixels × 768 pixels). Then, the system produces and projects the corresponding patterns in every subregion by dynamic switching of the exposure window in the order marked in figure 5(*a*), and the motorized stage moves synchronously with the exposure window across the image mask. The stitching of four adjacent subregions (i.e. nos 7, 8, 17 and 18 subregions in figure 5(*a*)) is realized by specifying an overlap region between every two adjacent subregions. These overlap regions (the stitching sides and corners) are generated by setting the moving distance of the stage to be shorter than the side length of the subregion. Thus, the stitching sides are subjected to two exposures, and the stitching corners are subjected to four exposures. In order to achieve seamless stitching, the grayscale values of these overlap regions should be carefully determined.

Figure 5(*b*) shows the exposure intensity measured at the surface of the photoresist film when the system projects patterns that are fully filled with different gray shades (red = green = blue = 105–255, with an interval of 10). We found that the measured exposure intensity approaches zero when the grayscale value is below 135. However, as the grayscale value increases to be larger than 135, the exposure intensity is observed to increase with the grayscale value. This curve is valuable for the regulation of grayscale values used in the overlap regions.

In addition to the grayscale value of the overlap region, another important parameter, i.e. the pixel size of this region, has to be determined before experiments. Although the pixel

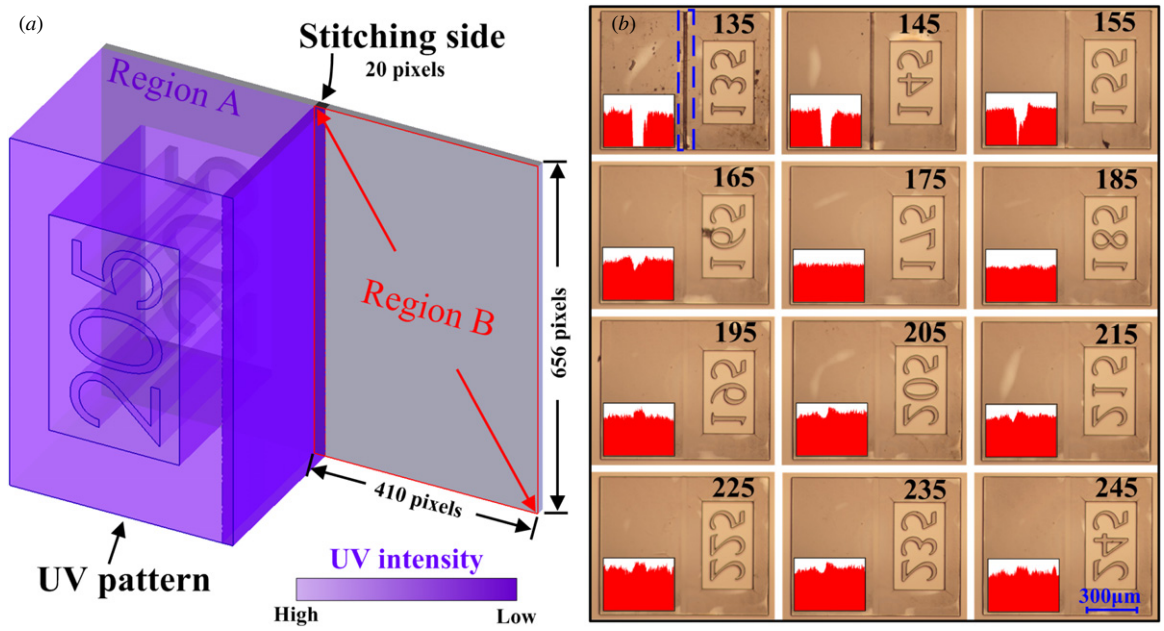

Figure 6. Effects of the stitching side's grayscale value on stitching quality. (*a*) Schematic diagram of the mask design used for exploring the optimum grayscale value of the stitching side. The whole mask consists of two exposure subregions (regions A and B). The pixel dimension of the stitching region is 20 pixels. The numbers embedded in the mask design denote the detailed grayscale values used in the stitching region. (*b*) Microscope images of the microstructure obtained using different grayscale values of the stitching side. The red inset figures, which show the variation spectrums of grayscale values across the stitching regions, are used for determining the optimum grayscale value.

size of the overlap region does not affect the dimension of the integral microstructure, a too small-sized overlap region may lead to the detachment of two adjacent subregions while an oversized overlap region may significantly add to the number of the dipartite subregions, resulting in the decrease of fabrication efficiency. In this work, we set this parameter at 20 pixels to avoid these problems. Then, we used the image mask depicted in figure 6(*a*) to explore the effects of the stitching side's grayscale value on the stitching quality. The whole image mask (656 pixels × 800 pixels) is divided into two subregions with the same dimension (region A and region B, 656 pixels × 410 pixels), generating an overlap region of 20 pixels in the middle. As the integral dimension of the structures in this mask approaches the millimeter level, the exposure time is determined to be 65 s according to the above analyses. By referring to the data depicted in figure 5(*b*), the grayscale value of the overlap region is gradually increased from 135 to 245 with an interval of 10. Microscopic images of the microstructures obtained from exposure experiments using these grayscale values are depicted in figure 6(*b*). The variation spectrums of the grayscale value measured across the stitching regions are used to assist in evaluating the stitching quality (see the red insets in figure 6(*b*)). As can be seen from these figures, sunken defects apparently exist in the stitching regions when the grayscale value of the stitching side is set at 135, 145 or 155. These defects can be attributed to the insufficient cross-linking of the photoresist under these low grayscale values. With the increase of the grayscale value, the sunken defects gradually become indistinct. As the grayscale value increases to 175 or 185, near-seamless stitching of regions A and B is achieved (there are no apparent oscillations in the variation spectrums). Overexposure is found to have but less impact on the stitching quality than underexposure. We observed that the cumulative exposure intensity measured in the stitching region using the mask fully filled with the optimum grayscale is nearly equal to the single exposure intensity measured using an all-white mask. With increasing the grayscale value, the cumulative exposure intensity turns to exceeding the intensity of a single exposure, resulting in overexposure of the photoresist and visibility of the stitching vestige. Finally, we determined the optimum grayscale value of the stitching side to be 178 by repeating this experiment with a small increment of this value.

After the grayscale value of the stitching side was determined, we used the same scheme to explore the optimum grayscale value of the stitching corner and study the effects of this value on the stitching quality. The detailed image mask (800 pixels × 656 pixels) used in this experiment is illustrated in the inset of figure 7. The whole mask is designed to be divided into four subregions. The pixel dimensions of each subregion and stitching side are specified to 608 pixels × 496 pixels and 200 pixels, respectively. Thus, a square stitching corner with a dimension of 200 pixels × 200 pixels is generated. The grayscale value of the stitching side is fixed at 178, while the grayscale value of the stitching corner is gradually increased from 135 to 185 with an interval of 10. The obtained microscope images are depicted in figure 7. From this figure, we found that defects exist apparently in the stitching region when the grayscale value of the stitching corner is set at 135 and 145. After the grayscale value is increased to be larger than 155, these defects gradually become indistinct. The measured exposure intensity is ∼3 mW cm^{-2} when using the

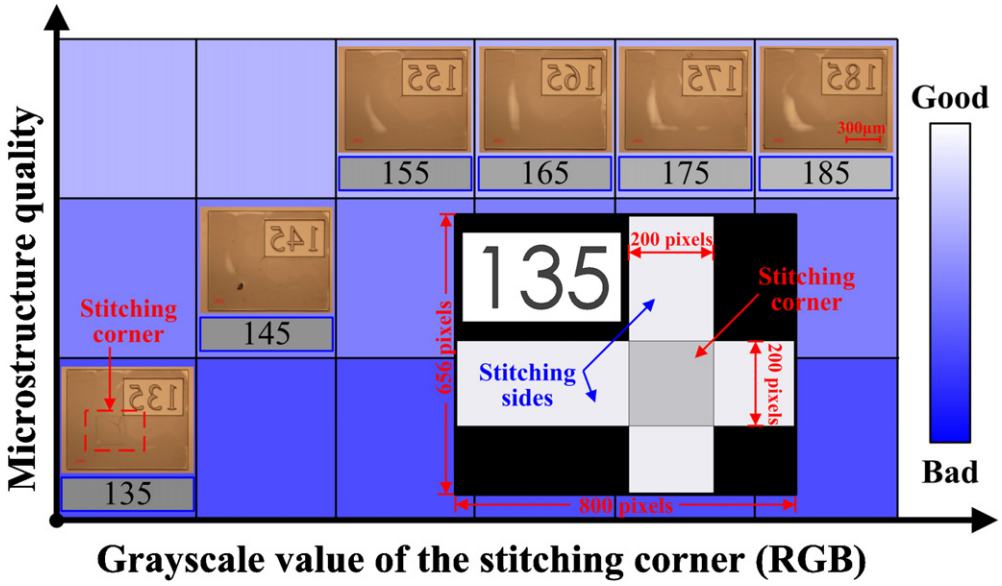

Figure 7. Effects of the stitching corner's grayscale value on the stitching quality. The horizontal abscissa shows the detailed grayscale values of the stitching corners, and the vertical ordinate presents different levels of the microstructure quality. These levels are distinguished by different shades of blue. Microscope images of the microstructure obtained using different grayscale values of the stitching corner are distributed into these levels. The inset shows the image mask (800 pixels × 656 pixels) used for exploring the optimum grayscale value of the stitching corner. The pixel dimension of the generated stitching corner is 200 pixels × 200 pixels.

mask with a grayscale value of 155. This indicates that the cumulative exposure intensity (four times, ∼12 mW cm^{-2}) suffered by the stitching corner significantly surpass the normal exposure intensity (∼10 mW cm^{-2}). Nevertheless, we found that the excessive exposure dose has little impact on the stitching quality. Therefore, we selected 155 as the optimum grayscale value for the following device fabrication process.

4. Application

In order to validate the applicability of the explored processing parameters, we fabricated and characterized several types of PDMS devices with straight or curved microchannels (figure 8). These devices which can be used for passive hydrodynamic manipulation of micro/nanomaterials typically require high-quality microstructures. Specifically, figures 8(*a*) and (*b*) illustrate two novel spiral microchannels with different dimensions. These microchannels can be employed to realize high-throughput focusing, separation and filtration of particles/cells based on the secondary flow and inertial migration induced in the unique spiral microchannels [36, 37]. Inset (i) in figure 8(*a*) illustrates the detailed cross-sectional profile of this microchannel. The observed good verticality under optimum processing parameters satisfies the demand of the rectangular cross-section for precise and efficient manipulation. Inset (ii) in figure 8(*b*) depicts the microscope image of this microchannel's planar structures. No serrate margins are observed in curved microchannels, and the exposure subregions realize dislocation-free and seamless stitching, overcoming the problem of edge roughness arising from the limited resolution of the printed transparency mask [11]. Moreover, we carried out an experimental study to validate the functional properties of the device illustrated in figure 8(*b*). Briefly, aqueous fluorescent polystyrene microparticles with a diameter of 5 μm (G0500, Thermo Fisher Scientific, Inc.) and a volume concentration of ∼0.015% were pumped through the spiral microchannel by using a programmable syringe pump (KDS201, KD Scientific, Inc.) at a flow rate of 220 μl min^{-1}. The motions of the flowing microparticles were recorded by using an inverted fluorescence microscope (IX71, Olympus) attached with a CCD camera (Exi Blue, Qimaging). The experimental results show that a single fluorescent stream is observed in the composite image (inset (iii) in figure 8(*b*)) obtained by overlaying a stack of 100 images, and when the external driving force of the sample suspension is turned off, the microparticles are restored to random distribution across the microchannel width (inset (iv) in figure 8(*b*)). These findings are in agreement with those reported in previous research works [36, 37]. A more comprehensive study disclosing the detailed dynamics of differently sized microparticles in this microchannel structure can be found in our group's recent work [38]. Figures 8(*c*) and (*d*) depict another two asymmetric contraction–expansion array microchannels which also apply the distinctive fluid effects to a high-throughput manipulation of microparticles/cells [39, 40]. The microscope image (top view, inset (v) in figure 8) and the SEM image (side view, inset (vi) in figure 8) of the master mold illustrated in figure 8(*c*) indicate that the complexly structured microchannel fabricated using the explored processing parameters has the approving quality.

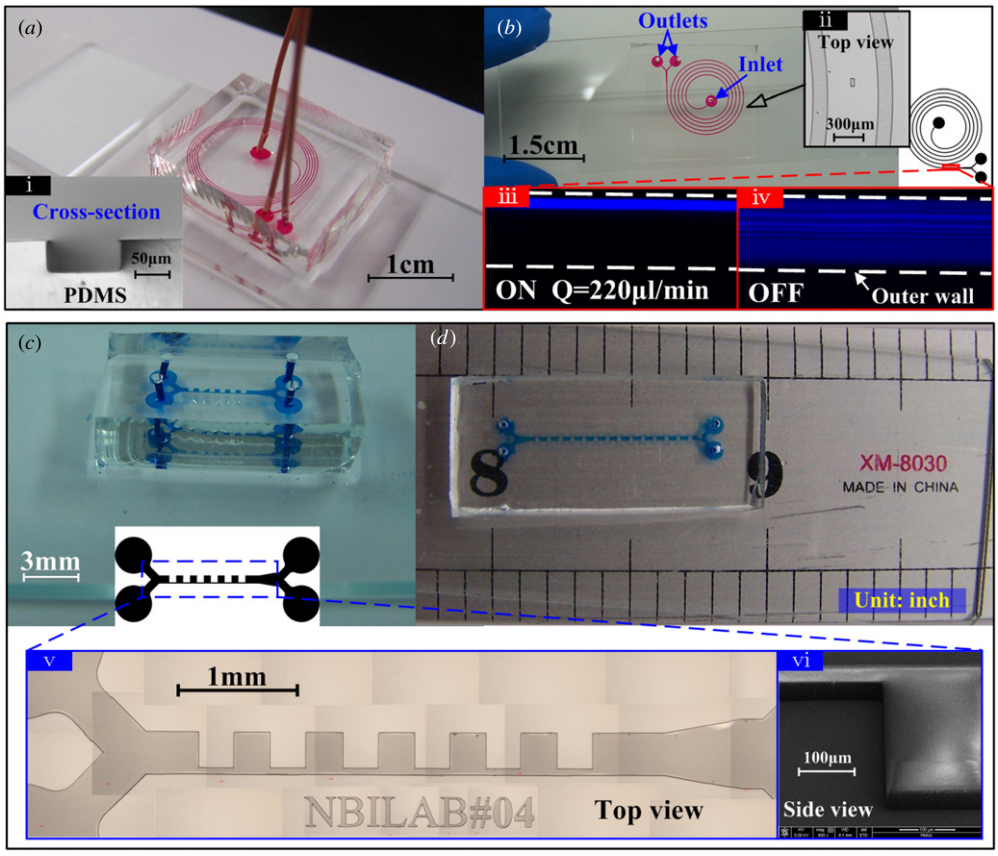

Figure 8. Microfluidic devices with various microchannel configurations fabricated using the PDMS molding technique. (*a*) An inertial microfluidic device with a five-loop Archimedean spiral microchannel (the microchannel width $W_1 = 80$ μm, height $H_1 = 50$ μm, initial radius $R_1 = 6$ mm and the spacing between two adjacent loops $D_1 = 220$ μm). Inset (i) shows the cross-sectional profile of this microchannel. (*b*) A spiral microchannel with different dimensions ($W_2 = 150$ μm, $H_2 = 50$ μm, $R_2 = 3.5$ mm, $D_2 = 500$ μm). Inset (ii) shows the microscope image of this microchannel's planar structures. Insets (iii) and (iv) show the fluorescent stream images captured near the outlet region at the flow rate of 220 and 0 μl min^{-1} (the syringe pump is turned off), respectively. (*c*) A contraction–expansion array microchannel (the dimension of the entire device is 8.9 mm $\times$ 3.7 mm, with contraction regions of 300 μm $\times$ 50 μm and expansion regions of 300 μm $\times$ 300 μm). Insets (v) and (vi) depict, respectively, the microscope image of the corresponding master mold's planar structures and the side-wall SEM image. (*d*) A contraction–expansion array microchannel with different dimensions (the dimension of the entire device is 19 mm $\times$ 3.7 mm, with contraction regions of 300 μm $\times$ 50 μm and expansion regions of 700 μm $\times$ 300 μm).

5. Conclusions

We propose maskless lithography as a potential and valuable method for rapidly and cost-effectively fabricating prototype microfluidic devices in laboratories. This method uses the DMD to modulate the spatial light and project an UV micropattern for exposing the photoresist film, avoiding the use of physical masks.

In this work, we conduct a systematic experimental investigation of the effects of exposure time on microstructure quality and dimension. The minimum exposure time was defined and used to rapidly fabricate microstructures whose dimensions and cross-sectional shapes are not stringently required, significantly improving their fabrication efficiency. Through qualitative evaluation and accurate measurement of the fabricated microstructures' quality and actual dimension, we find that the minimum or optimum exposure time decreases with the increase of the characteristic dimension. These results can be valuable for the dynamic and precise regulation of the microstructure features.

Then, we use the subregion stitching technique and sequential exposure process to fabricate larger microstructures. The relationship between grayscale value of the loaded image mask and the projected light intensity is established, and detailed effects of the stitching regions' grayscale value on the stitching quality are explored. These results may have great influence on the exploration of grayscale and multi-step lithography.

Finally, using master molds fabricated under the optimum process condition and the PDMS molding technique, various types of hydrodynamic microdevices are successfully fabricated. Their microstructure features and functions are characterized and validated.

Acknowledgments

This research work was supported by the Major Program of the National Natural Science Foundation of China (91023024), the National Natural Science Foundation of China (51145009), the National Basic Research Program of China (2011CB707601), the Specialized Research Fund for the Doctoral Program

of Higher Education (20110092110003) and the Jiangsu Graduate Innovative Research Program (CXZZ_0138).

References

[1] Waldbaur A, Rapp H, Lange K and Rapp B E 2011 *Anal. Methods* **3** 2681–716
[2] Abgrall P and Gué A-M 2007 *J. Micromech. Microeng.* **17** R15
[3] Becker H and Gärtner C 2008 *Anal. Bioanal. Chem.* **390** 89–111
[4] Selvaraj H, Tan B and Venkatakrishnan K 2011 *J. Micromech. Microeng.* **21** 075018
[5] Iliescu C, Taylor H, Avram M, Miao J and Franssila S 2012 *Biomicrofluidics* **6** 016505
[6] Lin C-H, Lee G-B, Lin Y-H and Chang G-L 2001 *J. Micromech. Microeng.* **11** 726
[7] Martinez A W, Phillips S T and Whitesides G M 2008 *Proc. Natl Acad. Sci. USA* **105** 19606–11
[8] Becker H and Locascio L E 2002 *Talanta* **56** 267–87
[9] McDonald J C and Whitesides G M 2002 *Acc. Chem. Res.* **35** 491–9
[10] Ng J M K, Gitlin I, Stroock A D and Whitesides G M 2002 *Electrophoresis* **23** 3461–73
[11] Duffy D C, McDonald J C, Schueller O J A and Whitesides G M 1998 *Anal. Chem.* **70** 4974–84
[12] Wilson M E, Kota N, Kim Y, Wang Y, Stolz D B, LeDuc P R and Ozdoganlar O B 2011 *Lab Chip* **11** 1550–5
[13] Shiu P P, Knopf G K, Ostojic M and Nikumb S 2008 *J. Micromech. Microeng.* **18** 025012
[14] Verma M K S, Majumder A and Ghatak A 2006 *Langmuir* **22** 10291–5
[15] Ma J, Jiang L, Pan X, Ma H, Lin B and Qin J 2010 *Microfluid. Nanofluid.* **9** 1247–52
[16] Stephan K, Pittet P, Renaud L, Kleimann P, Morin P, Ouaini N and Ferrigno R 2007 *J. Micromech. Microeng.* **17** N69
[17] Sudarsan A P and Ugaz V M 2004 *Anal. Chem.* **76** 3229–35
[18] Dang T-D, Kim Y H, Choi J H and Kim G-M 2012 *J. Micromech. Microeng.* **22** 015017
[19] Sharma C S, Sharma A and Madou M 2010 *Langmuir* **26** 2218–22
[20] Waldbaur A, Waterkotte B, Schmitz K and Rapp B E 2012 *Small* **8** 1570–8
[21] Singh-Gasson S, Green R D, Yue Y, Nelson C, Blattner F, Sussman M R and Cerrina F 1999 *Nature Biotechnol.* **17** 974–8
[22] Naiser T, Mai T, Michel W and Ott A 2006 *Rev. Sci. Instrum.* **77** 063711
[23] Lee H, Kim J, Kim H, Kim J and Kwon S 2010 *Nature Mater.* **9** 745–9
[24] Chung S E, Park W, Park H, Yu K, Park N and Kwon S 2007 *Appl. Phys. Lett.* **91** 041106
[25] Kim H, Kim J, Kim E-G, Heinz A J, Kwon S and Chun H 2010 *Biomicrofluidics* **4** 043014
[26] Rammohan A, Dwivedi P K, Martinez-Duarte R, Katepalli H, Madou M J and Sharma A 2011 *Sensors Actuators* B **153** 125–34
[27] Totsu K, Fujishiro K, Tanaka S and Esashi M 2006 *Sensors Actuators* A **130–1** 387–92
[28] Kobayashi J, Yamato M, Itoga K, Kikuchi A and Okano T 2004 *Adv. Mater.* **16** 1997–2001
[29] Itoga K, Kobayashi J, Tsuda Y, Yamato M and Okano T 2008 *Anal. Chem.* **80** 1323–7
[30] Zhao S, Cong H and Pan T 2009 *Lab Chip* **9** 1128–32
[31] Leigh S Y, Tattu A, Mitchell J S B and Entcheva E 2011 *Biomed. Microdevices* **13** 375–81
[32] Love J C, Wolfe D B, Jacobs H O and Whitesides G M 2001 *Langmuir* **17** 6005–12
[33] Sun C, Fang N, Wu D M and Zhang X 2005 *Sensors Actuators* A **121** 113–20
[34] Arora A, Simone G, Salieb-Beugelaar G B, Kim J T and Manz A 2010 *Anal. Chem.* **82** 4830–47
[35] Nilsson J, Evander M, Hammarström B and Laurell T 2009 *Anal. Chim. Acta* **649** 141–57
[36] Bhagat A A S, Kuntaegowdanahalli S S and Papautsky I 2008 *Lab Chip* **8** 1906–14
[37] Russom A, Gupta A K, Nagrath S, Di Carlo D, Edd J F and Toner M 2009 *New J. Phys.* **11** 075025
[38] Xiang N, Chen K, Sun D, Wang S, Yi H and Ni Z 2012 *Microfluid. Nanofluid.* at press
[39] Lee M G, Choi S, Kim H-J, Lim H K, Kim J-H, Huh N and Park J-K 2011 *Appl. Phys. Lett.* **98** 253702
[40] Hur S C, Mach A J and Di Carlo D 2011 *Biomicrofluidics* **5** 022206